Numerical Study of Fuselage Impact on Acoustic Characteristics of a Helicopter Rotor[*]

Ilya V. Abalakin[1] iD, *Vladimir G. Bobkov*[1] iD, *Tatiana K. Kozubskaya*[1] iD

The paper presents the results of the simulation of unsteady turbulent flow generated by helicopter main rotor in the presence of the fuselage with an emphasis on the analysis of the influence of the fuselage on the rotor-induced flow and the rotor-generated acoustic field. The Reynolds-averaged Navier–Stokes equations with the Spalart–Allmaras turbulence model are used to simulate the Caradonna–Tung rotor and ROBIN fuselage interaction in hovering flight. The governing equations are discretized using the vertex-centered control volume method on mixed-element unstructured meshes with the sliding mesh technology to treat the rotor. The acoustic field generated by the rotor+fuselage interaction is comparatively analyzed against the case of an isolated rotor. It is found that the presence of fuselage significantly changes the rotor-generated acoustics. In particular, the presence of the fuselage noticeably distorts the directivity of acoustic radiation and increases the overall sound pressure level under the fuselage up to 20 dB, emphasizing the importance of the influence of fuselage on the helicopter acoustics.

Keywords: rotorcraft, CFD, rotor-fuselage interaction, RANS, sliding mesh, supercomputer.

Introduction

A growing number of publications [1–5] focusing on the influence of fuselage on the helicopter rotor aerodynamcis demonstrate the importance of the subject. Recently, due to increasingly stringent International Civil Aviation Organization (ICAO) requirements on the permissible noise levels produced by aircrafts, including helicopters, the focus of research has shifted from rotor aerodynamics to the acoustics generated by the rotor in the presence of fuselage [6–9]. The simulation of the acoustics of the entire helicopter including the fuselage presents a challenge as it requires substantial computational resources and efficient parallel algorithms.

Due to significant difference in the relative fuselage and blade velocities the aerodynamic noise generated by the flow around fuselage is negligible compared to the sound of helicopter rotor. However, the fuselage can strongly influence the rotor acoustics and its directivity diagram. This paper focuses on the numerical investigation of the influence of a fuselage on the tonal acoustics of the helicopter main rotor. For that purpose a higher-accuracy method for aeroacoustic simulations of rotor-fuselage interaction is developed.

The hovering helicopter flight is modelled by the Caradonna–Tung rotor [10] and ROBIN fuselage [11, 12], scaled to be compatible with the rotor radius. The choice of the helicopter model is motivated by the availability of detailed geometrical descriptions, experimental results, and prior experience simulating these separate cases [13].

When developing a method for numerical simulation of rotor-fuselage interaction the approach should be capable of modeling flows in the presence of both stationary and moving/rotating objects. The flow over an isolated helicopter rotor can be easily simulated in a non-inertial reference frame associated with the rotor [14, 15] using non-deformable fixed computational mesh. The simultaneous presence of moving (helicopter rotor) and stationary (fuselage) components makes it impossible to use a mono-block mesh. A standard solution is to

---

use sliding meshes, i.e., the decomposition of mesh into two or more subdomains with sliding non-overlapping interfaces one of which (the one containing the fuselage) being stationary in absolute reference frame while the rest of them rotating with rotors. In the present work, we exploit this approach placing the main rotor into the rotating puck-shape subdomain. Despite the fact that the approach is widely used [14, 16, 17], the application of vertex-centered higher-accuracy schemes brings additional difficulties in approximating the fluxes at the sliding interfaces. To handle this problem, an earlier developed technique presented in [18] is used.

In this work, turbulent flow over an isolated rotor and a rotor interacting with a fuselage in hovering flight including the near field acoustics for both cases is considered. The results are compared, and the influence of the fuselage on the acoustic field is evaluated.

The paper is organized as follows. In Section 1, the problem of fuselage influence on the rotor tonal acoustics in hovering mode is formulated. The geometry of both components (i.e., the rotor and fuselage) are described, all the physical parameters are given. The governing mathematical model, the numerical methods in use and the computational set-up are presented in Sections 2, 3 and 4 respectively. Section 5 is devoted to the discussion of the obtained numerical results and to their comparative analysis. The concluding remarks and the acknowledgements are given at the end of the paper.

1. Problem Formulation

Turbulent flow over two-component configuration, consisting of two-bladed rotor and scaled fuselage model (Fig. 1) is considered. The rotor is modelled by the widely known Caradonna–Tung model [10], while the fuselage is approximated by the scaled version of ROBIN fuselage model [11, 12].

(a) Rotor and fuselage geometry   (b) Rotor and fuselage surface mesh
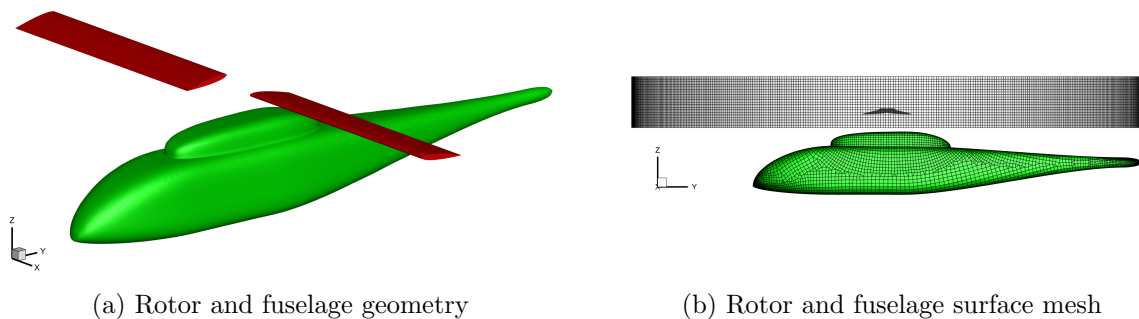
Figure 1. The case geometry and surface mesh

The rotor radius is $R = 1.143\ m$. The blades are based on the NACA 0012 airfoil and are untwisted and untapered. The blade chord is $0.1905\ m$ and the collective pitch angle is $8°$. A length of the ROBIN fuselage is scaled to $2R$. The distance between the rotor plane and the fuselage center of mass is $0.35\ m$. The gap between the fuselage pylon top and the rotor plane is about $0.125\ m$. The hovering flight is considered with the rotor rotation frequency $650\ RPM$, corresponding to the tip velocity $77.8\ m/s$. The Reynolds number defined in terms of rotor radius, tip velocity, the reference density $\rho_0 = 1.2046\ kg/m^3$, and molecular viscosity $\mu_0 = 1.8148 \times 10^{-5}\ Pa \cdot s$ is $Re = 5.9 \times 10^6$.

In addition to the aerodynamic characteristics, the pressure pulsation is measured in three sets of probes, namely the probes azimuthally distributed with angular step $10°$ in three planes including the rotor rotation plane (Fig. 2). The distance from each point to the rotor center is $2R$.
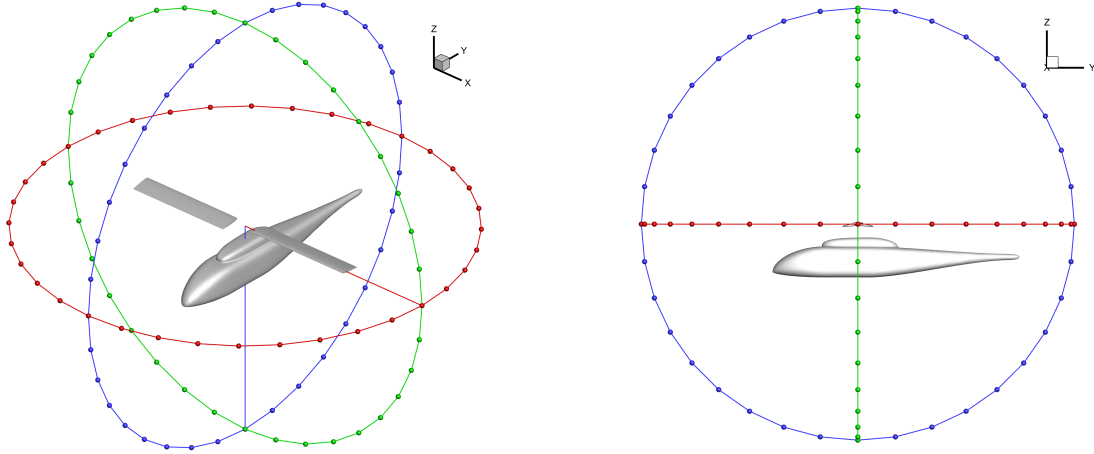
Figure 2. The sets of probes for acoustic field measurements: red – XY plane, green – XZ plane, blue – YZ plane

2. Governing Equations

The turbulent flow over the helicopter rotor is modelled by the unsteady Reynolds-averaged Navier–Stokes (RANS) equations with the closure model following the Boussinesq hypothesis. To simulate the turbulent flow near the rotor or rotor interacting with fuselage, the computational domain is decomposed in two subdomains, namely, a fixed subdomain considered in the absolute frame of reference (AFR) and a subdomain in the rotating frame of reference (RFR) that includes the rotor. The rotation velocity of RFR is taken equal to the angular velocity of rotor such that the rotor stationary in this frame of reference. In the fixed subdomain, the flow is governed by the RANS equations written in the AFR. To simulate the flow over the rotor, the unsteady RANS equations written in the RFR with the angular velocity $\boldsymbol{\omega}$ in terms of velocity vector defined in the AFR are solved. Both systems are closed by the Spalart–Allmaras turbulence model [19] governing the evolution of effective coefficient of turbulent viscosity. The unsteady RANS equations both in the AFR with $\boldsymbol{\omega} = 0$ and the RFR with $\boldsymbol{\omega} \neq 0$ have the following form:

$$
\begin{aligned}
&\frac{\partial \rho}{\partial t} + \operatorname{div} \rho \left(\mathbf{u} - \mathbf{V}\right) = 0, \\
&\frac{\partial \rho \mathbf{u}}{\partial t} + \operatorname{Div} \rho \left(\mathbf{u} - \mathbf{V}\right) \bigotimes \mathbf{u} + \nabla p = \operatorname{Div} \mathbf{P} - \rho \left(\boldsymbol{\omega} \times \mathbf{u}\right), \\
&\frac{\partial \rho E}{\partial t} + \operatorname{div} \rho \left(\mathbf{u} - \mathbf{V}\right) E + \operatorname{div} \mathbf{u} p = \operatorname{div} \mathbf{q} + \operatorname{div} \mathbf{P} \mathbf{u}, \\
&\frac{\partial \rho \widetilde{\nu}}{\partial t} + \operatorname{div} \rho \widetilde{\nu} \mathbf{u} = D_\nu + G_\nu - Y_\nu,
\end{aligned}
\tag{1}
$$

where $\mathbf{u}$ is the velocity vector, ρ is the density, $E = \frac{\mathbf{u}^2}{2} + \varepsilon$ is the total energy, ε is the specific internal energy, p is the pressure defined by ideal gas equation $p = (\gamma - 1)\rho\varepsilon$, $\gamma = 1.4$ is the specific ratio, d is the distance to the solid wall. In the system (1) $\mathbf{V}$ denotes the linear tangential velocity defined as $\boldsymbol{\omega} \times \mathbf{r}$ where $\mathbf{r}$ is the radius-vector. $\mathbf{P}$ is the viscous stress tensor defined by the strain rate tensor $\mathbf{S}$ according to the Boussinesq hypothesis in the following way:

$$
P_{ij} = 2\mu_{eff}\left(S_{ij} - \frac{1}{3}\frac{\partial u_i}{\partial x_i}\delta_{ij}\right), \quad S_{ij} = \frac{1}{2}\left(\frac{\partial u_i}{\partial x_j} + \frac{\partial u_j}{\partial x_i}\right),
$$

where the effective viscosity coefficient μ_{eff} equals to the sum of the coefficient of molecular viscosity μ and the turbulent eddy viscosity μ_T. Vector $\mathbf{q}$ defines the internal energy flux as[2]

$$q_i = \frac{\mu_{eff}}{\gamma \Pr} \frac{\partial \varepsilon}{\partial x_i},$$

where $\Pr = \frac{\mu_{eff} C_p}{\lambda}$ is the Prandtl number.

The coefficient of molecular viscosity μ is prescribed by the Sutherlands law

$$\mu = \mu_0 \frac{T_0 + S}{T + S} \left(\frac{T}{T_0} \right)^{\frac{3}{2}}, \ S = 120° K,$$

where μ_0 and T_0 are the molecular viscosity and the free stream temperature.

The last equations of system (1) describe the evolution of the variable $\widetilde{\nu}$ used to calculate turbulent eddy viscosity $\mu_T = \rho f_{\nu 1} \widetilde{\nu}$. A specific form of the terms D_ν, G_ν and Y_ν describing the diffusion, turbulence generation and turbulence destruction as well as the definitions of the damping function $f_{\nu 1}$ and corresponding constants can be found, for instance, in [19].

For further considerations, it should be noted that, from the standpoint of an observer in the stationary frame of reference, the system of equations (1) describes the evolution of conservative variables due to their transport in the rotating (with velocity $\mathbf{V}$) media, the pressure gradient and the velocity vector turn to the angle equal to $\boldsymbol{\omega} t$ (implemented by the term $- \rho (\boldsymbol{\omega} \times \mathbf{u})$ in the momentum equation). Note that in the numerical implementation of this system, the rotation velocity can be interpreted as the velocity of moving mesh.

To simplify further approximation within finite-volume approach, the system of Reynolds-averaged Navier–Stokes equations (1) can be written in the following vector form with respect to the vector of conservative variables $\mathbf{Q} = (\rho, \rho \mathbf{u}, E, \rho \widetilde{\nu})^T$:

$$\frac{\partial \mathbf{Q}}{\partial t} + \nabla \cdot \left(\mathcal{F}^C (\mathbf{Q}) - \mathcal{F}^R (\mathbf{Q}) - \mathcal{F}^D (\mathbf{Q}, \nabla \mathbf{Q}) \right) = \mathbf{S} (\mathbf{Q}, \nabla \mathbf{Q}). \tag{2}$$

System (2) includes the composite vectors $\mathcal{F}^C$, $\mathcal{F}^R$ and $\mathcal{F}^D$, each component of which $\mathbf{F}_i^C$, $\mathbf{F}_i^R$ and $\mathbf{F}_i^D$ in coordinate direction x_i ($i = 1, 2, 3$) represents the convective transport, rotation transport and diffusion flux vectors, respectively. Operator $(\nabla \cdot)$ is the divergence operator.

The convective transport, rotation transport and diffusion flux vectors are given as a function of the physical variables ρ, $\mathbf{u}$, p, $\widetilde{\nu}$ and their gradients

$$\mathbf{F}_i^C (\mathbf{Q}) = (\rho u_i, \rho u_i \mathbf{u} + p \mathbf{I}, (E + p) u_i, \rho \widetilde{\nu} u_i)^T,$$
$$\mathbf{F}_i^R (\mathbf{Q}) = (\rho V_i, \rho u_i \mathbf{V}, E V_i, \rho \widetilde{\nu} V_i)^T,$$
$$\mathbf{F}_i^D (\mathbf{Q}, \nabla \mathbf{Q}) = \left(0, P_{i1}, P_{i2}, P_{i3}, P_{ij} u_j + q_i, \frac{3}{2} (\mu + \rho \widetilde{\nu}) \frac{\partial \widetilde{\nu}}{\partial x_i} \right)^T,$$

where $\mathbf{I}$ – is the identity matrix.

Vector $\mathbf{S} (\mathbf{Q}, \nabla \mathbf{Q})$ is a source term describing the influence of the external forces that are not related to the transfer processes of the target variables $\mathbf{Q}$:

$$\mathbf{S} (\mathbf{Q}, \nabla \mathbf{Q}) = \left(0, \rho (\boldsymbol{\omega} \times \mathbf{u}), 0, G_\nu (\mathbf{Q}, \nabla \mathbf{Q}) - Y_\nu (\mathbf{Q}, \nabla \mathbf{Q}) + \frac{c_{b2}}{\sigma} \nabla \widetilde{\nu} \cdot \nabla \widetilde{\nu} \right)^T.$$

---

[2]We consider polytropic gas, so the specific heat c_V does not depend on temperature and, consequently, the internal energy is a linear function on temperature, i.e., $\varepsilon = c_V T$.

Here $c_{b2} = 0.622$ and $\sigma = 2/3$ according to the [19]. Note that the definition of diffusion term D_ν of the Spalart–Allmaras equation uses the square of the gradient of variable $\widetilde{\nu}$ which is of non-divergent form. Due to the last detail, we include this term to the source in the conservation law (2).

3. Numercial Method

The space discretization of the Navier–Stokes equations is based on the vertex-centered formulation implying that all the variables are defined at the vertices of hybrid unstructured mesh. The mesh vertices are the centers of the dual mesh cells. The approximation of the convective fluxes of the Navier–Stokes equations is built within the finite-volume approach. A cell of the dual mesh serves as control volume for which the discrete conservation laws are written. Thus, each control volume contains only one mesh vertex and belongs to the agglomeration of mesh elements containing this vertex.

Note that the mesh in each subdomain in corresponding reference frame is considered stationary, i.e., a geometry of each mesh element and respective control volume are fixed in time. Since the rotating subdomain is described in the RFR, the mesh there is also fixed and rotates with the rotor as a single entity.

The Navier–Stokes equations (2) are approximated using the integral form of these equations. The integral form of the system (2) for the control volume (or computational cell) K_i associated with the vertex i in the vertex-centered formulation can be written in the following form:

$$
\int_{K_i} \frac{d\mathbf{Q}}{dt} dV + \int_{\partial K_i} \left(\mathcal{F}^C(\mathbf{Q}) \cdot \mathbf{n} - (\mathbf{V} \cdot \mathbf{n}) \mathbf{Q} \right) dS =
$$
$$
\int_{\partial K_i} \nabla \cdot \mathcal{F}^D(\mathbf{Q}, \nabla \mathbf{Q}) dV + \int_{\partial K_i} \mathbf{S}(\mathbf{Q}, \nabla \mathbf{Q}) dV, \tag{3}
$$

where ∂K_i is the boundary of control volume (or cell) K_i, $\mathbf{n}$ is the unit external normal to the boundary ∂K_i.

Let $|K_i|$ be the volume of computational cell, $\partial K_{ij} = K_i \cap K_j$ is the common part of boundaries of cells K_i and K_j (or segment), $N_1(i)$ is a set of nodes neighboring to the vertex i, $\overline{\mathbf{Q}}_i$ is the integral average of variable $\mathbf{Q}$ on the cell K_i. The approximation of the convective part of the Navier–Stokes equations (3) can be considered as an approximation of the Euler equations written in a form of conservation laws:

$$
\frac{d\overline{\mathbf{Q}}_i}{dt} = -\frac{1}{|K_i|} \int_{\partial K_i} \left(\mathcal{F}^C(\mathbf{Q}) \cdot \mathbf{n} - (\mathbf{V} \cdot \mathbf{n}) \mathbf{Q} \right) dS = \sum_{j \in N_1(i)} \int_{\partial K_{ij}} \left(\mathcal{F}^C \cdot \mathbf{n} - (\mathbf{V} \cdot \mathbf{n}) \mathbf{Q} \right) ds
$$
$$
\approx \sum_{j \in N_1(i)} \mathbf{h}_{ij} \left(\mathbf{Q}_{ij}^L, \mathbf{Q}_{ij}^R \right) |\mathbf{n}_{ij}|,
$$

where $\mathbf{h}_{ij} \left(\mathbf{Q}_{ij}^L, \mathbf{Q}_{ij}^R \right)$ is the numerical flux approximating the flux through the square of segment ∂K_{ij} on the base of Godunov-type schemes, and $|\mathbf{n}_{ij}|$ is the absolute value of oriented square of segment

$$
\mathbf{n}_{ij} = \int_{\partial K_{ij}} \mathbf{n} \, dS. \tag{4}
$$

The normal velocity of rotation (or, the velocity of moving mesh) is approximated an average on the segment as

$$V_{ij} = \frac{1}{|\mathbf{n_{ij}}|} \int_{\partial K_{ij}} \mathbf{V} \cdot \mathbf{n}\, dS. \tag{5}$$

The value of variables $\mathbf{Q}_{ij}^{L/R}$ taken from the left and right from segment ∂K_{ij} are determined by the quasi-one-dimensional edge-based reconstruction on the extended stencil [20–22] that results in increasing the accuracy order of approximation of convective fluxes. The extended stencil contains $2n + 1$ points, and not all of them coincide with the mesh nodes. In the last case, the values in such points are found by the linear interpolation on the corresponding faces of mesh elements which have the intersection with the straight edge ij – containing line.

The approximation of viscous fluxes given by the volume integral $\int_{\partial K_i} \nabla \cdot \mathcal{F}^D\left(\mathbf{Q}, \nabla \mathbf{Q}\right) dV$ in the Navier–Stokes equation (3) is implemented by the Galerkin method basing on the linear polynomials. The integral of source term $\mathbf{S}$ in the system (3) is approximated as a volume average as

$$\int_{K_i} \mathbf{S}\left(\mathbf{Q}, \nabla \mathbf{Q}\right) dV \approx |K_i|\, \mathbf{S}\left(\mathbf{Q}_i, (\nabla \mathbf{Q})_i\right),$$

where the derivatives of variables $(\nabla \mathbf{Q})_i$ including to the source $\mathbf{S}$ are approximated by the discrete nodal gradients defined as a weighted sum of gradients on the mesh elements having the common vertex in node i [23].

The time integration is carried out using the implicit three-layer scheme of the second approximation order followed by the Newton linearization of the space-discretized equations. At each Newton iteration to solve the system of linear equations we use the stabilized method of biconjugate iterations (BiCGSTAB) [24]. The details of this approach and its usage in simulations are discussed in [25].

The presence of the stationary fuselage and the rotating blades results in the necessity to use two mesh blocks containing stationary and moving objects correspondingly and, consequently, to provide a proper interaction between these blocks.

A standard solution in this situation is the usage of sliding meshes, i.e., the decomposition of the mesh in two or more subdomains, one of which is at rest in the AFR while the rest of them rotate with the rotors they contain.

For the element-centered finite-volume methods assuming the variable averaging over unstructured mesh elements, the formulation providing the mesh sliding can be written without significant loss of accuracy. For the vertex-centered schemes assuming the variable averaging over dual cells, it is much harder to develop a method without any loss of accuracy on the interface. For the vertex-centered schemes for unstructured meshes in the general case, there is no known solution capable to preserve the high accuracy on sliding meshes. Nevertheless, a loss of accuracy can be compensated by a better scheme resolution and local mesh refinement near sliding interfaces. The following two versions of sliding mesh interfaces [18] have been developed:

- interface separating fixed and rotating mesh blocks is plane (for instance, a circle, an annual segment or a plane);
- interface separating fixed and rotating mesh blocks is a lateral surface of a finite straight round cylinder.

As a result, the rotating domain can be a finite straight round cylinder that includes both possible types of interface, or, in other words, can have a puck-shaped configuration. Within the developed approach, the control volumes (dual cells) are built in a way that the agglomerations of cells in the fixed and rotation subdomains do not overlap and have the curvilinear sliding

surface as the only common part. The cell faces belong to the lateral surface and thereby have its curvilinear shape. After the dual cells are defined, we calculate the values of $\mathbf{n}_{ij}$ and V_{ij} following the formula (4) and (5) with account for possible curvilinear shape of the cell faces.

4. Computational Set-up

As it is mentioned above, two types of simulations are performed, namely, the simulation of the isolated rotor in the cylindrical rotating region with the sliding interface (rotor simulation (RS)) and the simulation of the same rotor supplemented by the fuselage (rotor+fuselage simulation (RFS)).
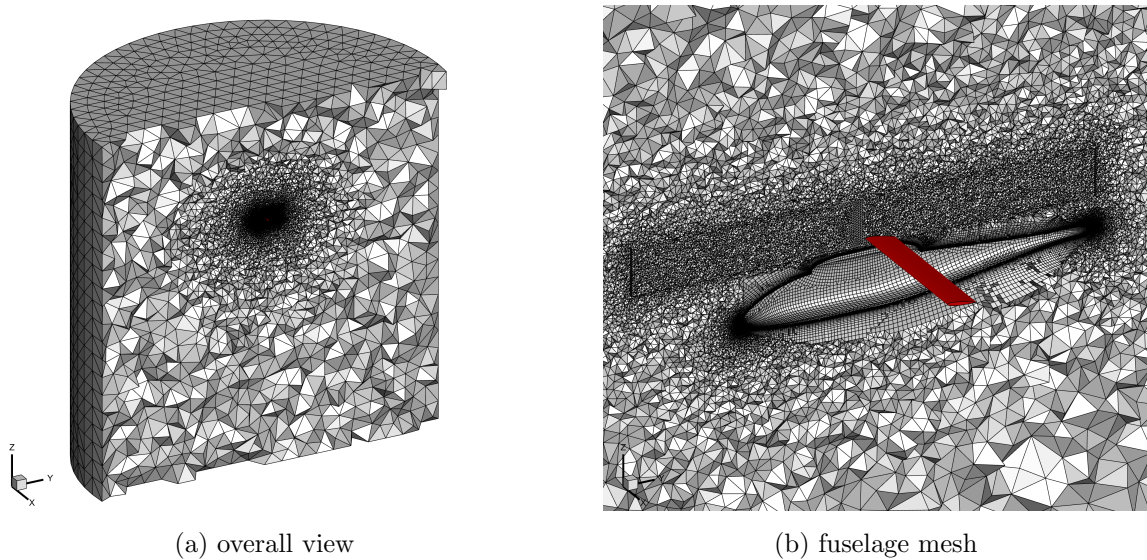
(a) overall view   (b) fuselage mesh
Figure 3. The unstructured mesh used in RFS case

For all the simulations, we build the mixed-element unstructured mesh consisting of tetrahedrons, prisms, pyramids and hexahedrons. In all the cases, the rotor surface mesh and the boundary layer prismatic mesh is the same, and the first surface cell height is chosen to meet the $y^+ < 1$ criteria. The sliding meshes represent two topologically separated mesh blocks: the outer fixed unstructured mesh block (Fig. 3a) and the inner rotating unstructured mesh block containing the rotor (Fig. 3b). The rotating puck-shaped domain is a cylinder with radius $1.5\ m$ and height $0.3\ m$. The maximum size of the mesh element inside the rotating region is limited by $15\ mm$. The computational domain in both simulations is a cylinder with radius $30\ m$ and height $60\ m$. The mesh sizes for both cases are represented in the Tab. 1.

Table 1. Computational mesh sizes

Case	Number of nodes	Number of cells
RS	6 820 497	21 360 814
RFS	7 156 503	21 773 730

The height of the mesh elements in the location of acoustic probes (see Sec. 1) is 8–10 cm that well resolves the BPF frequencies.

5. Numerical Results

## 5.1. Aerodynamic Characteristics of Isolated Rotor

The aerodynamic characteristics of Caradonna–Tung rotor in hover simulated in the RFR were predicted in our previous work [13]. The results showed a good agreement with the experimental data for pressure coefficient distribution and the tip vortex trajectory. Here we validate the AFR with sliding mesh approach on the same cases and obtain practically the same good results with respect to the available experimental data. Figure 4 demonstrates the pressure coefficient distribution in a set of the rotor blade sections.
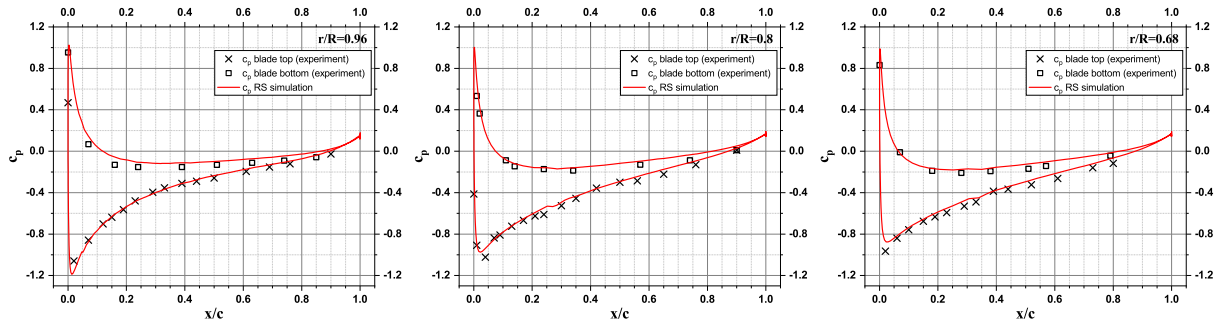
Figure 4. The pressure coefficient distribution: RS simulation in AFR vs. the experiment

5.2. Simulation of Turbulent Flow near Rotor+Fuselage Configuration

The flow field obtained in the RS presents a typical axial flow near a helicopter rotor (Fig. 5a–7a). The figures show the flow field and the wake behind the hovering rotor. The flow downstream the rotor is symmetrical as expected for the hovering mode. Besides, one can notice the slow vortex near the blades roots. The maxima of the velocity magnitude corresponds to the region of tip vortices with the downstream shift to the rotation axis.
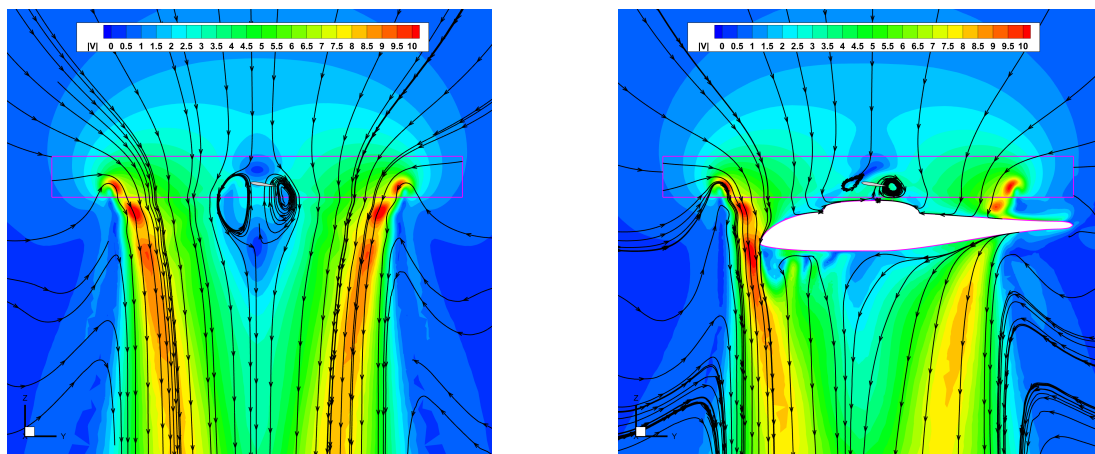

(a) RS case   (b) RFS case

Figure 5. The velocity magnitude field with streamlines in YZ section

Figure 5b shows that presence of the fuselage strongly affects the flow structure downstream the rotor. The flow becomes asymmetrical, and the most significant impact is the induced flow slowdown under the fuselage. The vorticity field indicates the intensive vortex shedding

downstream the fuselage body and the effect of interaction between the rotor tip vortices with the fuselage nose and its tail boom (see Fig. 6b, 7b).

(a) RS case   (b) RFS case
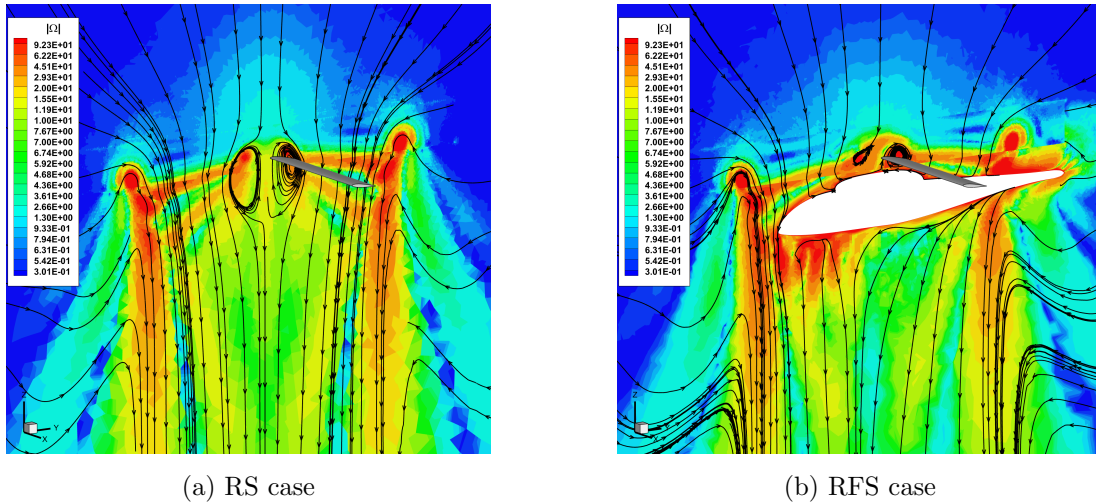
Figure 6. The vorticity magnitude field with streamlines in YZ section

As seen Fig. 7 with the Q-criterion visualization, both RS and RFS capture two revolutions of the wake spiral downstream the rotor.

(a) RS case   (b) RFS case
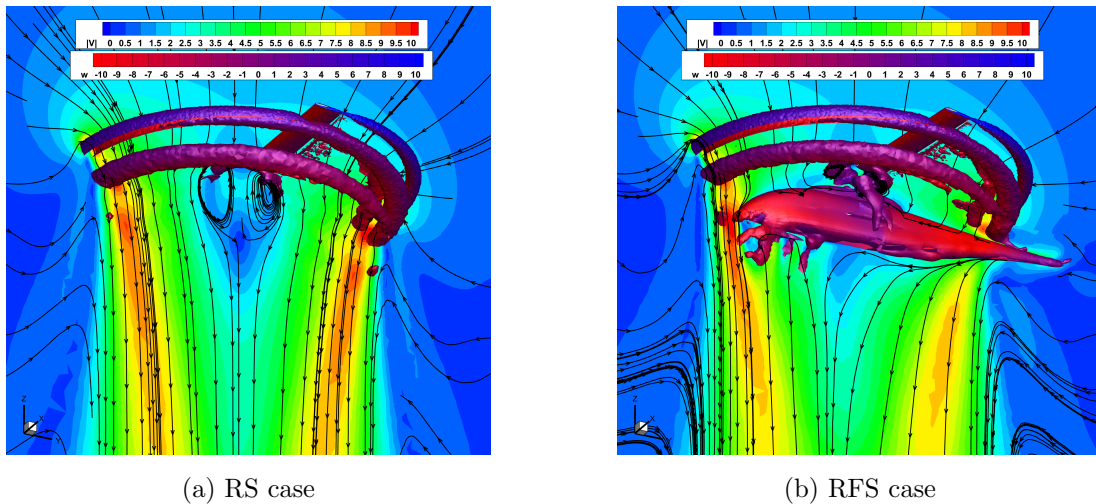
Figure 7. The velocity magnitude field with streamlines in YZ section and the Q-criterion iso-surface colored in the vertical flow velocity

5.3. Impact of Fuselage on Rotor Acoustics

The acoustic characteristics estimated basing on the simulation results are the spectra of pressure pulsation in the probes, and the directivity diagrams of blade passing frequency (BPF) sound pressure level (SPL) and overall sound pressure level (OASPL). The OASPL is determined by the pressure pulsations spectrum $P(\mathbf{x}, f)$ in the particular probes. The pressure pulsation spectrum is given by the Fourier transform of the function $p(\mathbf{x}, t)$ normalized by the quantity $p_0 = 2 \times 10^{-5} \ Pa$:

$$P(\mathbf{x}, f) = \frac{1}{2\pi} \int_{-\infty}^{+\infty} \frac{p(\mathbf{x}, t)}{p_0} e^{-i2\pi f} dt.$$

The total energy of the spectrum is calculated as the integral of the spectral power $S(\mathbf{x}, f) = P^2(\mathbf{x}, f)$: as

$$E(\mathbf{x}) = \int S(\mathbf{x}, f) \, dt,$$

where the integration is performed over all the resolvable frequencies. The OASPL measured in decibels is found by the formula

$$OASPL = 10 \log_{10} E(\mathbf{x}).$$

All the spectra presented are built using the fast Fourier transform on the probes pressure signals with $2\,Hz$ sampling frequency.

It should be noted that RANS method used in paper is capable to capture only the tonal acoustics, i.e., the acoustic harmonics at BPF and its multiples. In the setup for two-bladed rotor at $650\,RPM$, the BPF value is $21.6\,Hz$. The obtained spectrum of pressure pulsation in the probes confirms that the peak tonal frequencies are reached at the multiples of BPF (see Fig. 8). As expected, in plane XY of the rotor rotation the amplitudes of pressure pulsation in all the probes at BPF and its multiples have the same values (see Fig. 8a and Fig. 9a).

(a) XY plane   (b) YZ plane
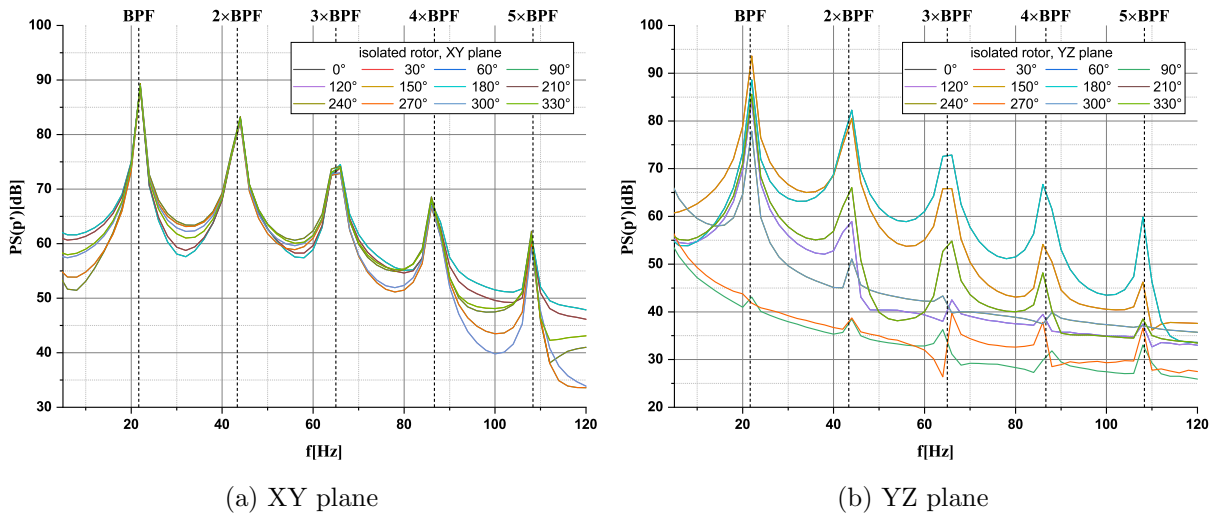
Figure 8. The pressure pulsation spectra measured in the probes obtained in RS

Figure 9 shows the directivity diagram of first BPF SPL in absence and presence of the fuselage at three orthogonal planes. The fuselage impact on the near-field acoustics is clearly seen. It should be noted that for the isolated rotor in hovering mode the pressure pulsation measured at the rotation axes must be zero theoretically. In our case, it is not so (it is about 40–$45\,dB$) solely because of the asymmetric computational setup. This fact is confirmed by our simulation of a single blade with the periodicity condition in azimuth where it is really zero (see [15]). The presence of the fuselage makes the configuration asymmetrical and it results in a slight asymmetry in the directivity diagram in planes XZ and YZ near the rotation axes. A noticeable SPL increase in comparison with the case of isolated rotor is also detected there. One can see up to $\sim 7\,dB$ amplitude growth at the $\pm 20°$ direction from the rotation axis in YZ plane and $\sim 7\,dB$ increase at azimuth $260° < \varphi < 290°$ in XZ plane. The difference in the directivity diagrams of first BPF SPL in the cases of isolated rotor and rotor with the fuselage is insignificant for the rest of azimuths.

Figure 10 demonstrates the directivity diagram of OASPL in absence and in presence of the fuselage in different planes. The asymmetry of the OASPL diagram in XZ and YZ planes due to
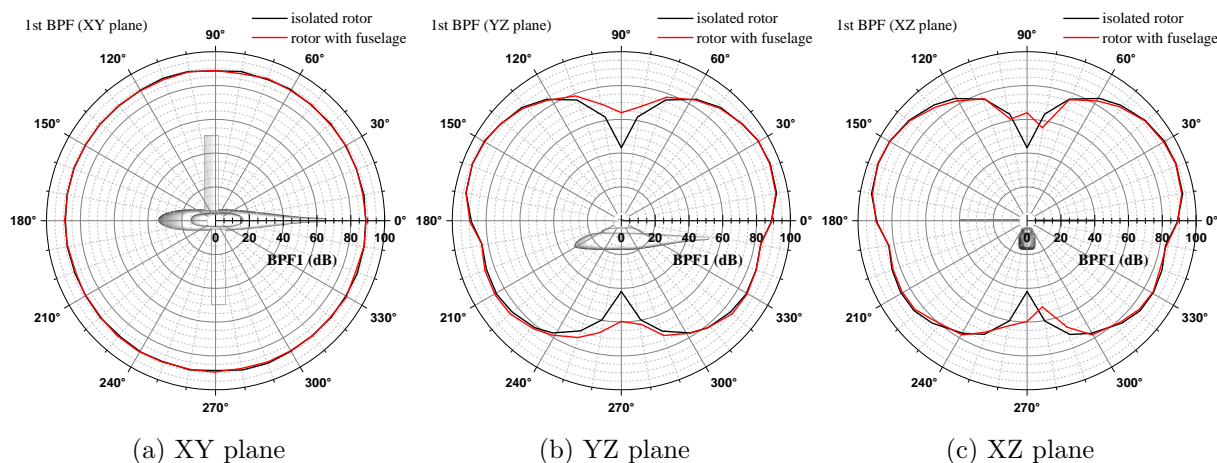
(a) XY plane   (b) YZ plane   (c) XZ plane

Figure 9. The directivity diagram of first BPF SPL

the fuselage presence becomes stronger in comparison with BPF SPL measurements. The OASPL near the rotation axes increases even more which can indicate a greater contribution of multiple frequencies. In YZ plane, the maximum difference observed on the azimuth $220° < \varphi < 300°$ and it reaches $\sim 20 \ dB$. In the XZ, plane the maximum difference observed on the azimuth $240° < \varphi < 300°$ and it reaches $\sim 19 \ dB$. Most likely, the reason of this OASPL symmetric growth is the blade interaction with the fuselage nose and tail boom at the azimuthal blade positions near $180°$ and $0°$ respectively (see Fig. 10a) that results in strengthening of scattering effects and, consequently, of acoustic radiation at multiple frequencies. In particular, it is seen that the azimuthal size of deformation of the directivity diagram is directly linked with the azimuthal size of the fuselage (see Fig. 10b, 10c).
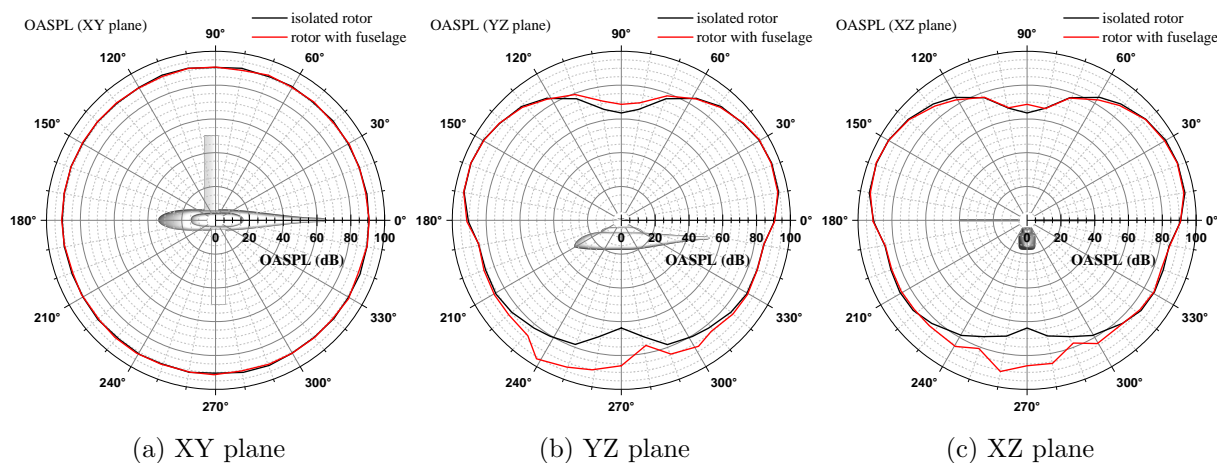

(a) XY plane   (b) YZ plane   (c) XZ plane

Figure 10. The OASPL directivity diagram

Conclusion

The paper presents the results of numerical simulation of tonal noise generated by the helicopter rotor and, which is more interesting, evaluates the impact of the fuselage on the generated acoustic field. It is shown that the presence of fuselage may significantly strengthen the acoustic radiation in the direction towards the ground and noticeably deform its directivity diagram. In particular, the most significant influence of the fuselage is detected at the probes in the low half of the diagram measured at two radiuses from the rotor center in vertical planes where

the OASPL growth reaches 20 dB. The discovered phenomenon of the possible amplification of acoustic radiation towards the ground due to the presence of the fuselage is of great importance for controlling the sound level generated by the helicopter. This result undoubtedly requires further study, and its thorough verification and validation.

The considered configuration "main rotor + fuselage" is an example of problems that are difficult to study in detail in wind tunnels. Field experiments related to the determination of the acoustic properties of entire helicopters are expensive and associated with the difficulties of accurate measurements in real operating conditions. In this situation, computational experiments may be in high demand. However, a natural obstacle on this way is the large computational resources required to compute such problems. This difficulty can be overcome or significantly mitigated by using modern high-performance systems with high efficiency, provided, for example, as in this work, by the efficient heterogeneous CPU + GPU parallelization model. The benefit of using HPC systems is further enhanced by the usage of higher-accuracy numerical methods and well-tuned mathematical models to accurately predict unsteady turbulent flows along with the generated acoustic fields.

Acknowledgements

References

1. Park, Y.M., Kwon, O.J.: Simulation of Unsteady Rotor Flow Field Using Unstructured Adaptive Sliding Meshes. Journal of the American Helicopter Society 49(4), 391–400 (2004). `https://doi.org/10.4050/JAHS.49.391`

2. Xu, H.-Y., Xing, S.-L., Ye, Z.-Y., Ma, M.-S.: A simple and conservative unstructured sliding-mesh approach for rotor-fuselage aerodynamic interaction simulation. Proceedings of the Institution of Mechanical Engineers, Part G: Journal of Aerospace Engineering 231(1), 163–179 (2017). `https://doi.org/10.1177/0954410016664919`

3. Steijl, R., Barakos, G.N.: Sliding mesh algorithm for CFD analysis of helicopter rotor-fuselage aerodynamics. Int. J. Numer. Meth. Fluids 58(5), 527–549 (2008). `https://doi.org/10.1002/fld.1757`

4. Steijl, R., Barakos, G.N.: Computational Study of Helicopter Rotor-Fuselage Aerodynamic Interactions. AIAA J. 47(9), 2143–2157 (2009). `https://doi.org/10.2514/1.41287`

5. Jung, M.-S., Kwon, O.-J.: Numerical Simulation of Unsteady Rotor Flow Using an Unstructured Overset Mesh Flow Solver. Int'l J. of Aeronautical, Space Sciences 10(1), 104–111 (2009). https://doi.org/10.5139/IJASS.2009.10.1.104

6. Goulos, I.: Modelling the aeroelastic response and flight dynamics of a hingeless rotor helicopter including the effects of rotor-fuselage aerodynamic interaction. The Aeronautical Journal 119(1214), 433–478 (2015). http://doi.org/10.1017/S0001924000010563

7. Cheng, Q., Zhu, Y., Feng, Z., Chen, Q.: A Coupled Helicopter Rotor/Fuselage Dynamics Model Using Finite Element Multi-body. MATEC Web Conf. 7, 01016 (2016). http://doi.org/10.1051/matecconf/20167701016

8. Kusyumov, A.N., Mikhailov, S.A., Garipova, L.I., *et al.*: Distribution of Acoustic Power Spectra for an Isolated Helicopter Fuselage. EPJ Web of Conferences 114, 02062 (2016). http://doi.org/10.1051/epjconf/201611402062

9. van der Wall, B.G., Yin, J.: A model for real-time computation of fuselage-rotor interference. International Journal of Modeling, Simulation, and Scientific Computing 08(04), 1743002 (2017). http://doi.org/10.1142/s1793962317430024

10. Caradonna, F.X., Tung, C.: Experimental and Analytical Studies of a Model Helicopter Rotor in Hover. Technical report, NASA Technical Memorandum TM-81232, 1981.

11. Freeman, C.E., Mineck, R.E.: Fuselage surface pressure measurements of a helicopter wind-tunnel model with a 3.15-meter diameter single rotor. Technical report, NASA Technical Memorandum TM-80051, 1979.

12. Hillier, B.B., Stock, M.J., Gharakhani, A. Robust and Corrected Coefficients for the ROtor-Body-INteraction Body. AIAA J. 59(10), 4281–4283 (2021). http://doi.org/10.2514/1.J060303

13. Bobkov, V. Abalikin, I., Kozubskaya, T.: Simulation of Helicopter Rotors on Unstructured Mixed Meshes Using Edge-Based Reconstruction Schemes. In 14th WCCM-ECCOMAS Congress, CIMNE (2021). http://doi.org/10.23967/wccm-eccomas.2020.308

14. Barakos, G., Vahdati, M., Sayma, A.I., *et al.*: A Fully Distributed Unstructured Navier–Stokes Solver for Large-Scale Aeroelasticity Computations, The Aeronautical Journal 105(1050), 419–426 (2016). http://doi.org/10.1017/S0001924000012392

15. Abalakin, I.V., Anikin, V.A., Bakhvalov, P.A., *et al.*: Numerical Investigation of the Aerodynamic and Acoustical Properties of a Shrouded Rotor. Fluid Dyn. 51(3), 419–433 (2016). http://doi.org/10.1134/S0015462816030145

16. Bachler, G., Schiffermller, H., Bregant, A.: A Parallel Fully Implicit Sliding Mesh Method for Industrial CFD Applications. Parallel Computational Fluid Dynamics 2000, 501–508 (2001). http://doi.org/10.1016/B978-044450673-3/50129-9

17. Titarev, V.A., Faranosov, G.A., Chernyshev, S.A., Batrakov, A.S.: Numerical Modeling of the Influence of the Relative Positions of a Propeller and Pylon on Turboprop Aircraft Noise. Acoust. Phys. 64, 760–773 (2018). http://doi.org/10.1134/S1063771018060118

18. Abalakin, I.V., Bakhvalov, P.A., Bobkov, V.G., Gorobets, A.V.: Parallel Algorithm for Flow Simulation in Rotor-Stator Systems Based on Edge-Based Schemes. Math. Models Comput. Simul. 13(1), 172–180 (2021). `http://doi.org/10.1134/S2070048221010026`

19. Spalart, P.R., Allmaras, S.R.: A One-Equation Turbulence Model for Aerodynamic Flows. 30th Aerospace Sciences Meeting, Exhibit, Reno, NV, USA, January 6–9, 1992. AIAA Paper 92-0439. `http://doi.org/10.2514/6.1992-439`

20. Abalakin, I., Bakhvalov, P., Kozubskaya, T.: Edge-based reconstruction schemes for unstructured tetrahedral meshes. Int. J. Numer. Meth. Fluids 81(6), 331–356 (2016). `http://doi.org/10.1002/fld.4187`

21. Bakhvalov, P.A., Kozubskaya, T.K.: Construction of edge-based 1-exact schemes for solving the Euler equations on hybrid unstructured meshes. Comput. Math. Math. Phys. 57(4), 680–697 (2017). `http://doi.org/10.1134/S0965542517040030`

22. Bakhvalov, P., Kozubskaya, T.: EBR-WENO scheme for solving gas dynamics problems with discontinuities on unstructured meshes. Comput. Fluids 157, 312–324 (2017). `http://doi.org/10.1016/j.compfluid.2017.09.004`

23. Dervieux, A., Alauzet, F., Loseille, A., Koobus, K.: Mesh Adaptation for Computational Fluid Dynamics 1: Continuous Riemannian Metrics and Feature-based Adaptation. ISTE-Wiley Publishing (2022). `http://doi.org/10.1002/9781394163991`

24. van der Vorst, H.A.: Bi-CGSTAB: A Fast and Smoothly Converging Variant of Bi-CG for the Solution of Nonsymmetric Linear Systems. SIAM J. Sci. Stat. Comput. 13(2), 631–644 (1992). `http://doi.org/10.1137/0913035`

25. Abalakin, I.V., Bobkov, V.G., Kozubskaya, T.K.: Implementation of the low Mach number method for calculating flows in the NOISEtte software package. Math. Models Comput. Simul. 9(6), 688–696 (2017). `http://doi.org/10.1134/S2070048217060023`

26. Gorobets, A., Bakhvalov, P.: Heterogeneous CPU+GPU parallelization for high-accuracy scale-resolving simulations of compressible turbulent flows on hybrid supercomputers. Computer Physics Communications 271, 108231 (2021). `http://doi.org/10.1016/j.cpc.2021.108231`

27. Gorobets, A.V., Duben, A.P.: Technology for Supercomputer Simulation of Turbulent Flows in the Good New Days of Exascale Computing. Supercomputing Frontiers and Innovations 8(4), 4–10 (2022). `http://doi.org/10.14529/jsfi210401`